Contents

Chapter 4

MiniBooNE Neutrino Flux Predictions

In this Chapter, predictions for the muon neutrino and electron neutrino fluxes at the MiniBooNE detector are presented. The program used to obtain the simulated neutrino fluxes, its physics assumptions, and the flux predictions are described in detail. Section 4.1 describes some generalities on the "beam Monte Carlo" code used; Section 4.2 discusses the simulation of the beamline geometry, materials, and of the primary proton beam; Sections 4.4, 4.5 and 4.6 summarize the physics input to the simulation for the processes of most direct relevance for producing muon and electron neutrinos at MiniBooNE; the flux predictions are given in Section 4.7 .

4.1   The beam Monte Carlo simulation code

4.1.1   Inputs to neutrino flux predictions

The purpose of the MiniBooNE beam Monte Carlo is to predict the fluxes at the MiniBooNE detector for all relevant neutrino species (ν_μ, $\bar{\nu}_\mu$, ν_e, $\bar{\nu}_e$) as a function of neutrino energy, per proton on target and per unit area, and to obtain an accurate

estimate of the associated flux systematic uncertainties. The flux understanding is of primary importance for most MiniBooNE analyses, including for example neutrino cross-section meaurements, and $\nu_\mu \to \nu_e$ and $\nu_\mu \to \nu_{\not\mu}$ oscillation analyses.

The MiniBooNE flux prediction makes use of physics inputs both external and internal to the experiment. The most important physics input that is external to MiniBooNE is meson production data in proton-Beryllium hadronic interactions for proton beam momenta in the $\sim$ 10 GeV/c range, since the flux uncertainty is dominated by the secondary meson production uncertainty. Therefore, the most important design requirement of the simulation tool developed at MiniBooNE for neutrino flux predictions is its flexible hadronic physics model interface.

In addition, the MiniBooNE data itself will provide inputs to the neutrino flux predictions. First, the observation of muon neutrinos at MiniBooNE will constrain the electron neutrino flux component due to muon decays. Second, neutrino fluxes from Kaon decays will be constrained by the measurement of muons from Kaon decays in the Little Muon Counters along the decay region.

4.1.2   Code structure

Currently, the combination of two simulations programs is used at MiniBooNE to obtain neutrino flux predictions. First, a GEANT4-based Monte Carlo code is responsible for simulating the chain of processes going from primary protons hitting the MiniBooNE target, until decays of mesons and muons yielding neutrinos occur. GEANT4 [2, 3] is a software package designed to accurately simulate the passage of particles through matter. In particular, the GEANT4 application used at MiniBooNE simulate: the geometry and the materials present in the MiniBooNE target hall and decay region; the physics processes governing the interactions of baryons, mesons and leptons involved in neutrino production; the generation of events, initiated by Booster primary protons specified according to their beam optics characteristics; the

tracking of particles through the materials present in the target hall and decay region, and through the horn magnetic field; the storage of simulated data at various levels of refinement, from single physics process information, to event-level information for the entire neutrino parentage history. A second, FORTRAN-based Monte Carlo code uses the output of the GEANT4 program as input, and is responsible for generating the neutrino kinematics distributions from meson and muon decays, and for obtaining the final neutrino fluxes extrapolated at the MiniBooNE detector with negligible beam Monte Carlo statistical error.

The physics interface of GEANT4 allows the user to choose among an abundant set of built-in models, and also to easily implement custom-defined process cross-sections and final state descriptions, making GEANT4 an ideal simulation toolkit for the MiniBooNE beam Monte Carlo. The class category hierarchy of the C++ based beam Monte Carlo code follows the schematics given in Fig. 4.1 (taken from [3]).

4.2   Simulation of beamline geometry, materials, and primary proton beam

4.2.1   Geometry and materials

The beam Monte Carlo program simulates the most relevant materials and volumes present in the target hall and decay region. In Fig.4.2, four images from the beamline geometry simulation are shown. The images show the entire decay region, and details of the target pile region, horn, and target. The volumes shown in red are made with Beryllium, the regions shown in blue with iron. The other two relevant materials are concrete from the decay region walls and for the collimator system located downstream of the horn, and Aluminum for the MiniBooNE horn.
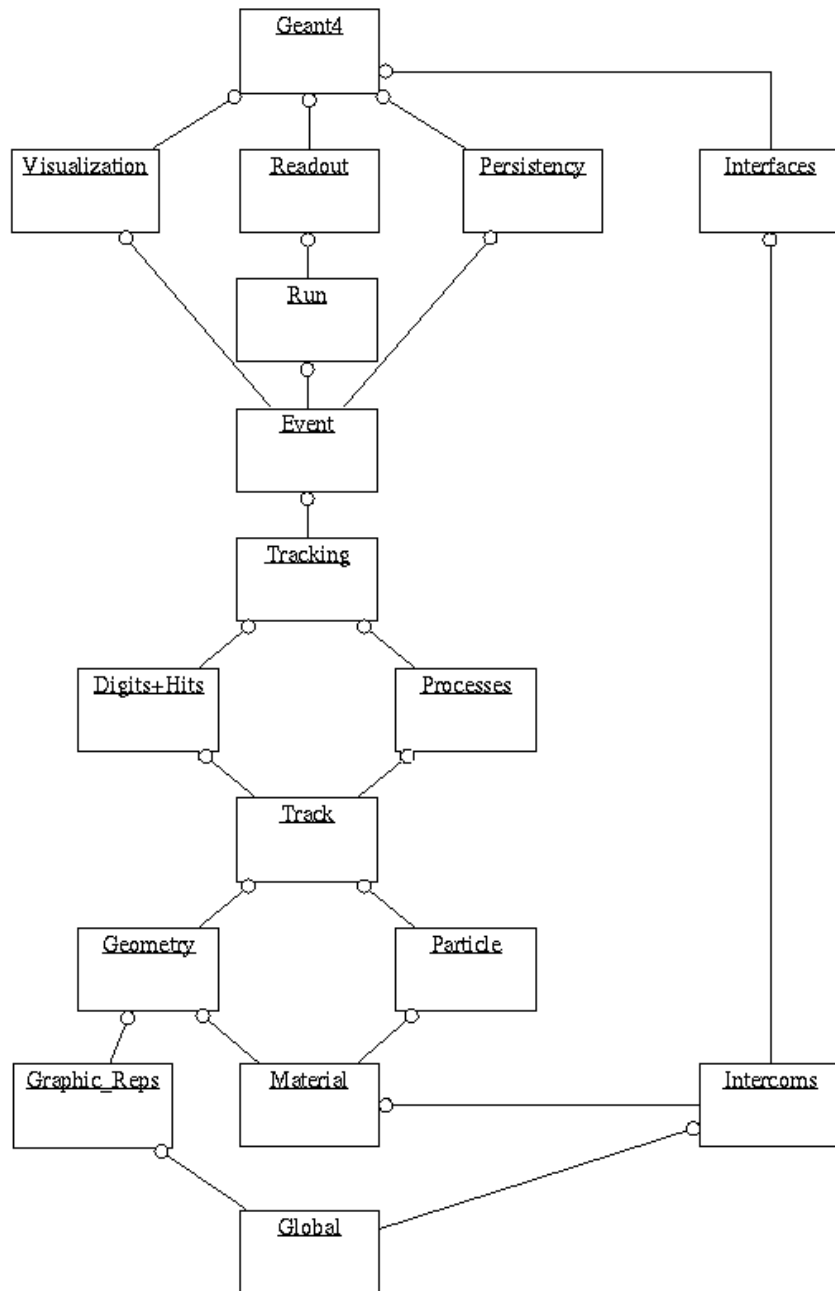
Figure 4.1: *GEANT4 class categories [3]. Each box represents a class category. The circle at the end of a straight line means that the class category which has this circle uses the other line-connected category.*
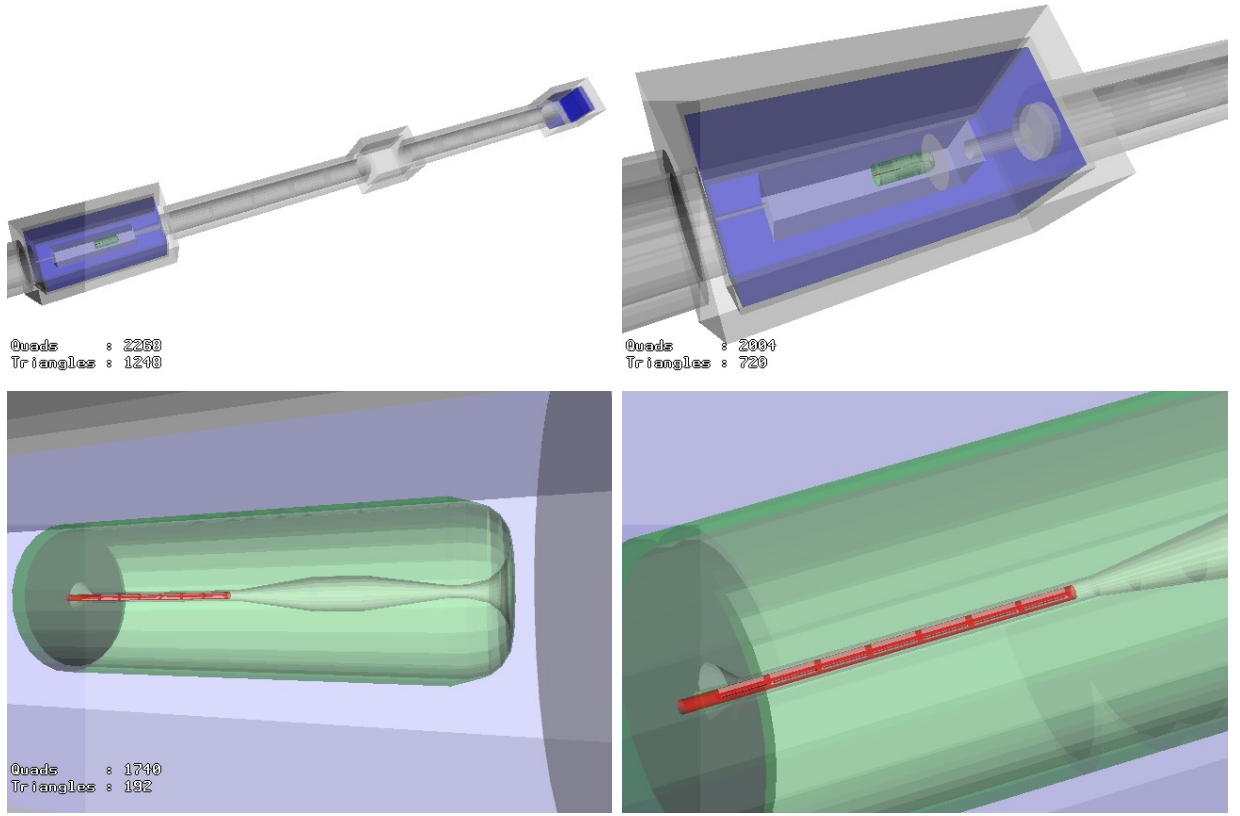
Figure 4.2: *The MiniBooNE beamline geometry implemented in the simulation. The pictures show the entire 50 m decay region, and details of the target pile region, horn, and target.*

4.2.2 Primary proton event generator

The event generator in the beam Monte Carlo simulation is very simple: all that is needed is to construct one primary proton per event with 8 GeV kinetic energy, directed towards the Beryllium target. To account for the fact that the beam optics is not perfect, some smearing in the initial transverse position (x, y) and angular divergence (θ_x, θ_y) of the beam is introduced, in the coordinate system where the z axis points along the beam direction, and y points upwards. Also, the mean (x_0, y_0) positions and the mean $(\theta_{x,0}, \theta_{y,0})$ directions of the primary beam can be changed for systematic study purposes, together with the longitudinal position z_0 for the primary

Parameter	x_0	σ_x	y_0	σ_y	$\theta_{x,0}$	$\sigma_{\theta,x}$	$\theta_{y,0}$	$\sigma_{\theta,y}$
Value	0	1.51 mm	0	0.75 mm	0	0.66 mrad	0	0.40 mrad

Table 4.1: *Beam optics parameters used in the beam Monte Carlo simulation. See text for definitions. The parameters correspond to an initial longitudinal position along the beam direction for the generated protons of z_0 =-1 cm, and to a coordinate system having the MiniBooNE Beryllium target located at: 3.5 cm $< z <$ 74.6 cm, $\sqrt{x^2 + y^2} <$ 4.76 cm.*

proton at birth; all beam optics parameters refer to this longitudinal position. The position and angular smearing are described by gaussian distributions. More specifically, the initial position and momentum of the generated primary proton are [1]:

$$
\begin{cases}
x = x_0 + \sigma_x \texttt{ran1} \\
y = y_0 + \sigma_y \texttt{ran2} \\
z = z_0 \\
p_x = \sqrt{E_p^2 - m_p^2}(\theta_{x,0} + \sigma_{\theta_x}\texttt{ran3}) \\
p_y = \sqrt{E_p^2 - m_p^2}(\theta_{y,0} + \sigma_{\theta_y}\texttt{ran4}) \\
p_z = \sqrt{E_p^2 - m_p^2 - p_x^2 - p_y^2}
\end{cases}
\tag{4.1}
$$

where `ran1`, `ran2`, `ran3`, `ran4` are four random numbers drawn from a gaussian distribution of mean zero and variance one, $E_p = K_p + m_p$, where K_p=8 GeV and m_p is the proton mass. The MiniBooNE beam optics parameters (x_0, σ_x, y_0, σ_y, z_0, $\theta_{x,0}$, σ_{θ_x}, $\theta_{y,0}$, σ_{θ_y}) used in the flux simulation are given in Tab. 4.1. These values are determined from detailed simulations of Booster protons in the 8 GeV Fermilab neutrino line, and cross-checked with measurements from several beam detectors measuring beam positions, directions, and profiles at various locations along the beamline. It is estimated that this choice of beam optics parameters yields a 99.8% targeting efficiency.

---

[1]The small-angle appropximation is assumed throughout the simulation of primary beam parameters.

Neutrino Flavor	ν_μ	$\bar{\nu}_\mu$	ν_e	$\bar{\nu}_e$
Flux fraction (%)	92.7	6.6	0.6	0.1

Table 4.2: *Neutrino flavor composition of the MiniBooNE neutrino flux in neutrino running, as predicted by the beam Monte Carlo simulation.*

4.3 Properties of typical neutrinos reaching the MiniBooNE detector

In Sections 4.4, 4.5, 4.6, we discuss several physics processes of relevance for MiniBooNE flux predictions. As an introduction to these Sections, we first discuss some properties of typical events yielding neutrinos at the MiniBooNE detector, as predicted by the beam Monte Carlo simulation. This Section gives some qualitative idea of what "relevant" means.

Table 4.2 shows the predicted neutrino flavor composition of the MiniBooNE neutrino flux in neutrino running mode. The flux is dominated by muon neutrinos, comprising 92.7% of the total neutrino flux, with a 6.6% flux contribution from muon antineutrinos. Electron neutrinos comprise about 0.6% of the total neutrino flux.

Table 4.3 shows the most likely "neutrino history" for neutrinos reaching MiniBooNE, divided per neutrino flavor. The muon neutrino flux is mostly (86.1%) due to the decay of positive pions, from pions that are in turn produced directly by inelastic interactions of primary protons. The contribution of muon neutrinos from pions created by secondary protons and neutrons is also non-negligible, as is non-negligible the contribution of muon neutrinos from charged Kaon decays. Electron neutrinos are dominated by the decays of muons produced by positive pions, which are in turn directly produced in inelastic interactions of primary protons (48.0% of the total electron neutrino flux). Contributions to the electron neutrino flux from charged and neutral Kaon decays, and from other muon decay chains, are also significant.

Neutrino flavor	Process	Flux fraction per flavor (%)
ν_μ	$p \to \pi^+ \to \nu_\mu$	86.1
	$p \to p \to \pi^+ \to \nu_\mu$	7.3
	$p \to K^+ \to \nu_\mu$	2.8
	$p \to n \to \pi^+ \to \nu_\mu$	1.9
	Other	1.9
$\bar{\nu}_\mu$	$p \to \pi^- \to \bar{\nu}_\mu$	55.0
	$p \to p \to \pi^- \to \bar{\nu}_\mu$	16.6
	$p \to n \to \pi^- \to \bar{\nu}_\mu$	12.0
	Other	16.4
ν_e	$p \to \pi^+ \to \mu^+ \to \nu_e$	47.6
	$p \to K^+ \to \nu_e$	32.7
	$p \to K^0_L \to \nu_e$	7.2
	$p \to p \to \pi^+ \to \mu^+ \to \nu_e$	5.0
	Other	7.5
$\bar{\nu}_e$	$p \to K^0_L \to \bar{\nu}_e$	65.5
	$p \to \pi^- \to \mu^- \to \bar{\nu}_e$	9.8
	Other	24.7

Table 4.3: *Most likely history for muon neutrinos reaching the MiniBooNE detector, as simulated by the beam Monte Carlo. The arrows indicate either an inelastic interaction, or a decay.*

The remaining two tables in this Section focus on muon neutrinos, and in particular on the $p \to \pi^+ \to \nu_\mu$ events that mainly contribute to the total muon neutrino flux. Table 4.4 lists average properties concerning pion production, focusing, and pion decay kinematics. Pions yielding muon neutrinos at MiniBooNE are produced in the Beryllium target with an average momentum and angle of ~ 2.2 GeV/c and ~ 100

Quantity	Description	Value
$\langle p_{\pi+,in} \rangle$	Initial π^+ momentum	2.17 GeV/c
$\langle \vartheta_{\pi+,in} \rangle$	Initial π^+ angle	106 mrad
$\langle l_{\pi+,B} \rangle$	π^+ path in horn field	82.1 cm
$\langle B_{\pi+} \rangle$	Horn field along π^+ trajectory	0.71 Tesla
$\langle p_{\pi+,fin} \rangle$	Final π^+ momentum	2.08 GeV/c
$\langle \vartheta_{\pi+,fin} \rangle$	Final π^+ angle	30 mrad
$\langle E_\nu \rangle$	Neutrino energy	0.762 GeV

Table 4.4: *Average properties for $p \rightarrow \pi^+ \rightarrow \nu_\mu$ processes giving muon neutrinos at Mini-BooNE, as simulated by the beam Monte Carlo. The properties in this Table illustrate pion production, focusing, and decay kinematics characteristics.*

mrad, respectively. Pions cross loose a small fraction of energy crossing various materials, and are focused by a ~ 1 Tesla horn magnetic field over distances of the order of ~ 1 meter, as well as by the collimator system, resulting in average pion angles at decay of about 30 mrad. Neutrinos reaching the MiniBooNE detector are produced forward in the pion centerof-mass frame, resulting in typical neutrino energies that are a little less than the maximum neutrino energy of $E_\nu = (m_\pi^2 - m_\mu^2)E_\pi/m_\pi^2$, where m_π and m_μ are π^+ and μ^+ masses, respectively, and E_π is the total π^+ energy at decay.

Table 4.5 shows other properties for $p \rightarrow \pi^+ \rightarrow \nu_\mu$ events yielding muon neutrinos at MiniBooNE, related to beamline geometry, energy loss, and pion decay characteristics. Primary protons travel about 22 cm on average in the Be target before producing positive pions. The pions that are produced by protons can interact via several physics processes (see Sections 4.4, 4.5) while crossing few centimeters of Beryllium and Aluminum materials, before decaying into neutrinos after typical pathlengths of 20 m in air.

In the following Sections 4.4, 4.5, 4.6, we quantify the agreement between the

Particle	Material	$\langle \Delta E \rangle$ (MeV)	$\langle l \rangle$ (cm)
p	Beryllium	56.3	22.3
π^+	Aluminum	22.3	5.9
π^+	Beryllium	21.5	8.5
π^+	Iron	11.3	1.1
π^+	Concrete	6.5	2.9
π^+	Air	2.9	1900

Table 4.5: *Average properties for $p \rightarrow \pi^+ \rightarrow \nu_\mu$ processes giving muon neutrinos at Mini-BooNE, as simulated by the beam Monte Carlo. The properties in this Table illustrate beamline geometry, energy loss, and pion decay characteristics, and are classified per beamline material. In the Table, $\langle E \rangle$ is the average particle energy loss, and $\langle l \rangle$ is the average particle pathlength in the material.*

physics inputs to the beam Monte Carlo simulation, with expectations drawn from experimental data points, data-driven parametrizations, and theoretical predictions. Each physics input is tested individually, by disabling all other physics processes in the simulation.

4.4 Hadronic Interactions

4.4.1 Inelastic interactions of primary protons in the Mini-BooNE target

An accurate simulation of inelastic interactions of primary protons in the MiniBooNE target material is essential for obtaining accurate neutrino flux predictions. For this reason, a custom-defined description of both the total proton-Beryllium inelastic cross-section, and of the final state for these inelastic interactions, is used at Mini-

BooNE.

The proton-Beryllium total inelastic cross-section assumed in the simulation for 8.9 GeV/c Booster protons is σ_{inel} =189.3 mb, as obtained from an interpolation of the cross-sections measured in the BNL E910 experiment at 6.4 and 12.3 GeV/c proton beam momenta [4]. This value corresponds to an inelastic interaction length for protons in Beryllium of λ_{inel} =42.3 cm. The impact of varying this cross-section value within its measured uncertainty is taken into account in the estimate of the flux systematic uncertainty.

Concerning the final state in inelastic proton-Beryllium interactions, the seven types of secondaries of most direct relevance for neutrino fluxes are simulated: π^+, π^-, K^+, K^-, K_L^0, protons and neutrons. For each inelastic interaction, the multiplicities and kinematic distributions for the first three particle types are drawn from three parametrizations of double-differential, inclusive production cross-sections described next, while production cross-sections obtained from MARS15 [5, 6] simulations are assumed for the latter four particle types.

The double-differential, inclusive production cross-sections for the secondaries $S = \pi^+$, π^-, K^+ are described according to "Sanford-Wang" parametrizations [7]:

$$\frac{d^2\sigma(p + Be \rightarrow S + X)}{dpd\Omega} = c_1 p^{c_2}(1 - \frac{p}{p_{beam} - c_9}) \exp[-c_3 \frac{p^{c_4}}{p_{beam}^{c_5}} - c_6\vartheta(p - c_7 p_{beam} \cos^{c_8} \vartheta)]$$

(4.2)

where X means any other particle in the final state, p_{beam} is the proton beam momentum in GeV/c, p and θ are the secondary momentum and angle in units of GeV/c and radians, respectively, $d^2\sigma/(dpd\Omega)$ is expressed in units of $mb/(GeV/c\ sr)$, and the parameters $c_1, \ldots, c_9$ are empirical parameters obtained from fits to meson production data. For pion production, the parameter c_9 is not fit, but set to one. The value of these parameters assumed by the beam Monte Carlo simulation are given in Tab. 4.6. Concerning muon (anti)neutrino fluxes, the simulation of π^+ production is particularly important in the current MiniBooNE neutrino running mode, while a correct π^- production simulation would be essential for a likely future MiniBooNE

Secondary	Sanford-Wang parameter								
Particle	c_1	c_2	c_3	c_4	c_5	c_6	c_7	c_8	c_9
π^+	206.4	1.030	5.902	2.012	2.127	5.510	0.9958E-01	12.03	
π^-	184.1	1.052	6.706	1.275	1.424	5.225	0.9439E-01	10.74	
K^+	12.53	1.654	0.314	1.038	0.174	4.658	0.106	10.53	2.635

Table 4.6: Values for the Sanford-Wang $\pi^\pm$ and K^+ production parameters used in the beam Monte Carlo simulation to describe meson production in proton-Beryllium interactions [4].

antineutrino run. On the other hand, the knowledge of K^+ production affects the estimate for the amount of intrinsic electron neutrinos in the beam from K^+ decays.

The Sanford-Wang parameters given in Tab. 4.6 are obtained from fits of meson production data from a number of hadro-production experiments, with proton beam momenta similar to the Booster proton momentum, and sensitive to a phase space for meson production of relevance to MiniBooNE. A summary of the data used in the MiniBooNE Sanford-Wang fits is given in Tab. 4.7.

While some data used in the MiniBooNE Sanford-Wang fits is available in the literature, the dominant contribution (in terms of statistical power) for $\pi^\pm$ production is based on a new analysis of Brookhaven E910 data at 6.4 and 12.3 GeV/c proton beam momenta on a thin Beryllium target, done by collaborators from both experiments. Figure 4.3 shows a comparison between E910 12.3 GeV/c data on π^+ production, and the parametrization assumed in the beam Monte Carlo simulation. In the near future, meson production data from the CERN HARP experiment [12], obtained with Beryllium targets of various thicknesses and at the Booster beam momentum, will also be used as inputs to the beam Monte Carlo simulation. The uncertainties in meson production data obtained from the Sanford-Wang fits are propagated into neutrino flux systematic uncertainties.

Given the assumptions described above, the particle multiplicities per inelastic

Secondary particle S	Proton beam momentum (GeV/c)	Secondary particle phase space				Data points	Ref.
		$\theta_{S,min}$ (mrad)	$\theta_{S,max}$ (mrad)	$p_{S,min}$ (GeV/c)	$p_{S,max}$ (GeV/c)		
π^+	12.3	42	331	0.6	5.4	71	[4]
	12.4	2	206	2.1	6.3	53	[7]
	6.4	71	353	0.6	4.2	29	[4]
	10.1	61	61	1.0	4.5	14	[8]
π^-	12.3	42	331	0.6	5.4	70	[4]
	12.4	2	206	2.1	6.3	32	[7]
	6.4	71	353	0.6	4.2	28	[4]
K^+	19.2	13	70	6.0	16.0	41	[9]
	12.3	0	175	0.5	1.0	9	[10]
	9.5	62	62	3.0	6.5	5	[11]

Table 4.7: *Summary of hadro-production data used to obtain the MiniBooNE, Sanford-Wang parametrizations of the double-differential, meson production inclusive cross-sections.*

Secondary particle type	π^+	π^-	K^+	K^-	K_L^0	p	n
Average multiplicity	0.799	0.596	0.048	0.003	0.030	1.544	1.341

Table 4.8: *Average multiplicity per inelastic collision for secondary particles produced in inelastic collisions of 8.9 GeV/c protons in the MiniBooNE Beryllium target.*

interaction for all simulated secondaries are given in Tab.4.8. The average multiplicities per inelastic collision are defined as the integral the double-differential, inclusive production cross-section over the entire secondaries phase space, divided by the total proton-Beryllium inelastic interaction. Proton and neutron productions are the most abundant, followed by π^+ production.

Figure 4.4 shows the one-dimensional projections along the longitudinal and transverse momentum components at production of the secondaries simulated in the
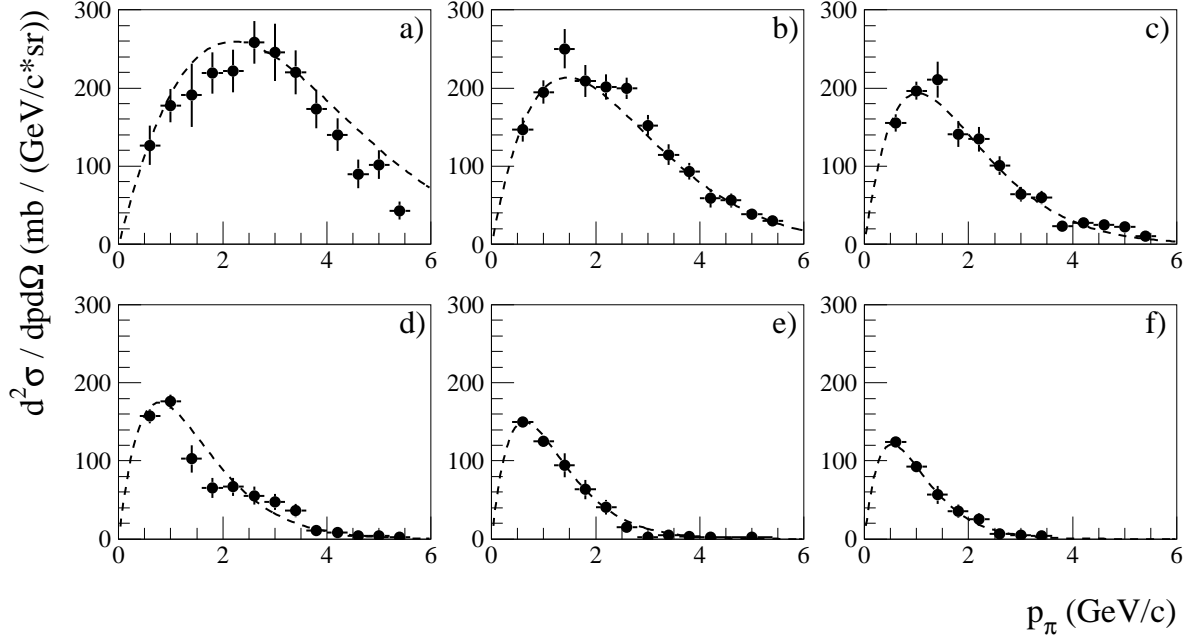
Figure 4.3: *The double-differential π^+ production cross-section in proton-Beryllium interactions, as a function of pion production momentum p_π and angle θ_π. The six panels correspond to: θ_π (mrad) = 42 (a), 95 (b), 153 (c), 212 (d), 272 (e), 331 (f). The points correspond to BNL E910 data at p_{beam} = 12.3 GeV/c [4]; the dashed lines correspond to the beam Monte Carlo π^+ production assumption, specified by Eq. 4.2 and Tab. 4.6, for the same 12.3 GeV/c beam momentum.*

interactions of 8.9 GeV/c protons in Beryllium, normalized per unit area. We note here the leading particle effect in the proton and neutron distributions, with momenta extending up to incident proton momentum, and that the pion kinematic distributions at production are peaked at considerably lower momenta compared to the typical momenta for pions yielding neutrinos directed toward the MiniBooNE detector (see Tab. 4.4).
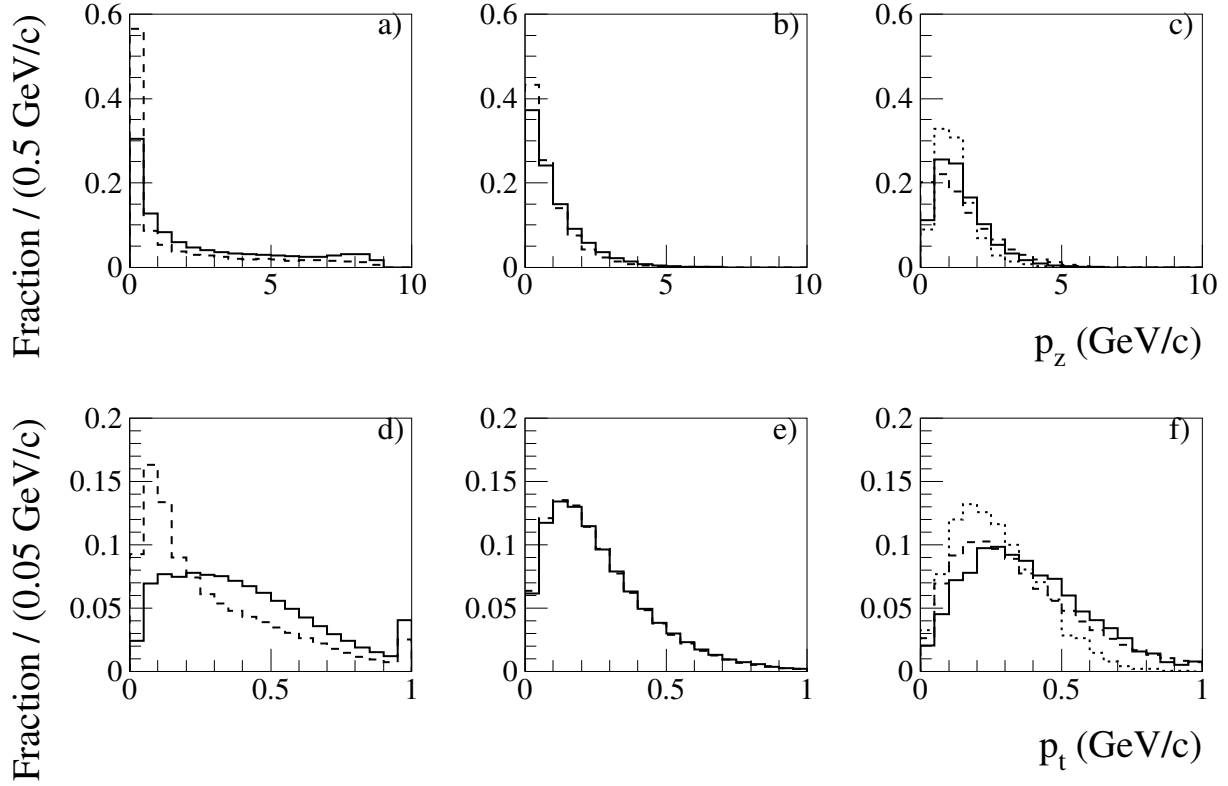
Figure 4.4: *One-dimensional projections along the longitudinal (top) and transverse (bottom) momentum components p_z and p_t of the double-differential production cross-sections for simulated secondaries from inelastic interactions of 8.9 GeV/c proton in Beryllium. All histograms are normalized to unit area. Panels a) and d) refer to baryon production: solid histograms for protons, dashed for neutrons; b) and e) to non-strange meson production: solid histograms for π^+, dashed for π^-; c) and f) to strange meson production: solid histograms for K^+, dashed for K^-, dotted for K_L^0.*

4.4.2 Other inelastic interactions

Secondary interactions of pions and protons also play a non-negligible role in determining the MiniBooNE neutrino flux. These particles, once they have been produced in a primary inelastic interaction, can still traverse significant amounts of target and horn material (relative to the inelastic interaction length, see Tab. 4.5), and in turn interact inelastically. Therefore, we describe here the simulation of inelastic interac-

tions of secondary pions and protons of various momenta in Beryllium and Aluminum.

These inelastic processes, with the exception of $K_p > 7.5$ GeV protons in Beryllium discussed in Section 4.4.1, are described by built-in GEANT4 physics models. The final state description model typically used in the simulations is part of the 'Low Energy Parametrization Driven Model", based on the GEANT3.21 GHEISHA package [3]. For the purposes of estimating flux systematic uncertainties, alternative built-in physics models have also been explored, namely the "Bertini Intranuclear cascade model", and the "binary cascade model" [3].

Figure 4.5 shows average properties of inelastic interactions of secondary π^+'s and protons in Beryllium and Aluminum, as a function of the projectile momentum. The average properties shown are the inelastic interaction length λ_{inel}, the average number $\langle N_\pi \rangle$ of π^+'s in the inelastic interaction final state, the average momentum $\langle p_\pi \rangle$ for final state π^+'s, and the average angle $\langle \theta_\pi \rangle$ between the incoming projectile and the outgoing final state π^+'s.

Experimental data are available on the total inelastic length, and are shown for comparison in Fig. 4.5. The inelastic interaction lengths for π^+'s and protons are similar, of the order of 40-50 cm. The inelastic cross-sections show a mild momentum dependence over the range $1 < p \ (GeV/c) < 10$.

Pions in the final state tend to be more numerous for higher energy projectiles, for π^+ projectiles than for p projectiles, and show little dependence on the target material. The average π^+ momenta tend to be much smaller than the projectile momenta, and π^+ emission angles are large.

4.4.3 Elastic interactions

Apart from scattering inelastically, pions and protons can also interact elastically in the target hall and decay region materials. Unlike the inelastic processes described above, no particle absorption, particle production, or charge exchange are present in
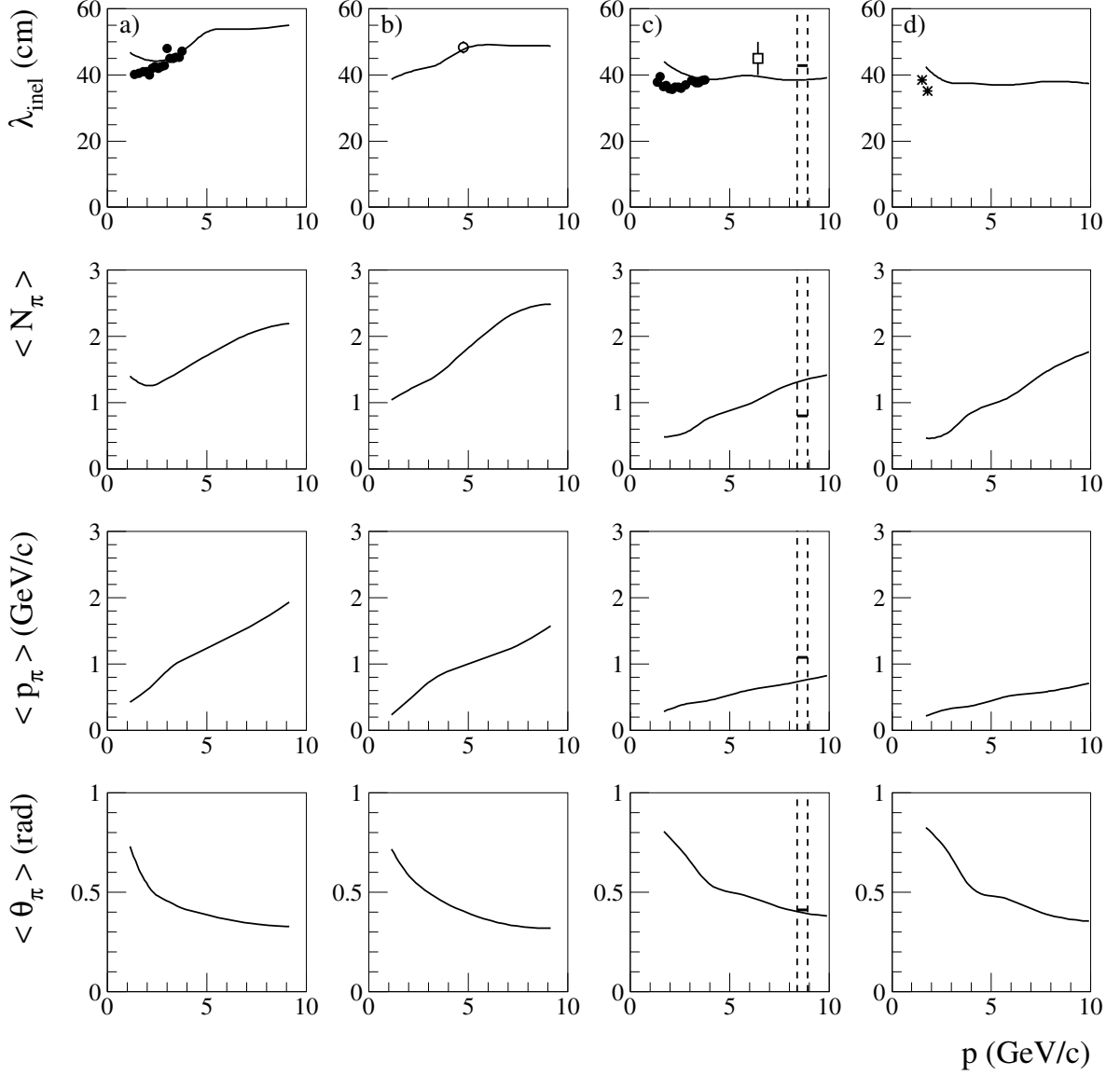
Figure 4.5: *Inelastic processes for π^+'s and protons interacting in Beryllium and Aluminum, as a function of the projectile momentum p. From left to right: inelastic π^+-Be, π^+-Al, p-Be, and p-Al processes. From top to bottom: inelastic interaction length λ_{inel}, and average number per inelastic collision $\langle N_\pi \rangle$, momentum $\langle p_\pi \rangle$ and angle with respect to the projectile direction $\langle \vartheta_\pi \rangle$, of final state π^+'s. The curves show the beam Monte Carlo assumptions, the points show experimental data: • from Ref. [13], ∘ from [14], □ from [4], ∗ from [15]. Moreover, the values within dashed lines in the p-Be panels show the assumptions adopted for primary protons, described in Section 4.4.1.*
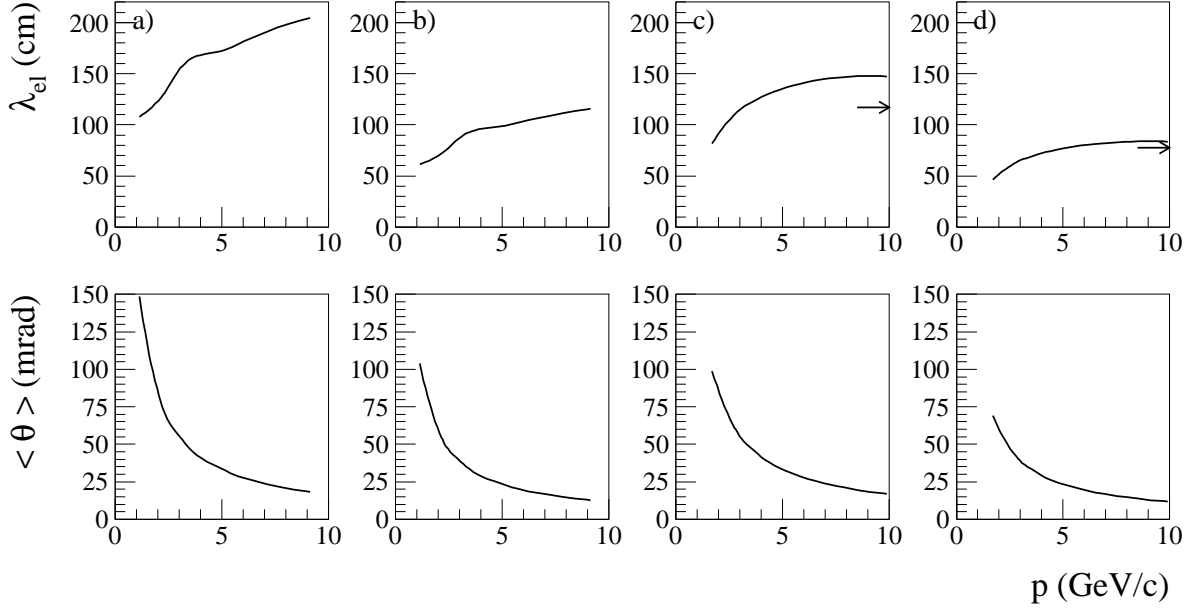
Figure 4.6: *Elastic processes for π^+ 'sd and protons interacting in Beryllium and Aluminum, as a function of projectile momentum p. From left to right: elastic π^+-Be, π^+-Al, p-Be, and p-Al processes. From top to bottom: elastic interaction length λ_{el}, and average projectile deflection angle $\langle\vartheta\rangle$. The arrows in the top plots indicate the high-energy values from [1].*

this case, and the only effect is an angular deflection of the projectile with respect to its original direction. In Figure 4.6, the elastic interaction length λ_{el} and the average elastic scattering deflection angle assumed by the beam Monte Carlo simulation are shown as a function of projectile momentum.

The elastic interaction length is smaller in Aluminum than in Beryllium, and similar for protons or pions; moreover, the elastic interaction length tends to increase with projectile momemtum, in the $1 < p\ (GeV/c) < 10$ momentum range. Over this range, typical values in Beryllium are 110-205 cm, and 45-115 cm in Aluminum. significantly larger than the corresponding inelastic interaction lengths. From the data in Ref. [1], and assuming that the total nuclear collision cross-section is given by the sum of the total elastic and inelastic cross-section, the elastic interaction length for > 60 GeV/c protons can be extracted. The elastic interaction length values from [1] are 117.0 and 77.7 cm in Beryllium and Aluminum, respectively, which are also

shown in Fig. 4.6.

The mean deflection angles are much smaller in elastic collisions than in the previously discussed inelastic collisions. The angles tend to be larger, on average, for low-energy projectiles, and are very similar for protons and pions. Typical deflection angles in one elastic collision are 10-150 mrad, and are therefore significant.

4.5   Electromagnetic processes

4.5.1   Particle trajectories in the MiniBooNE horn magnetic field

The horn magnetic field provides a large increase in flux: the neutrino rate at Mini-BooNE per proton on target has been measured to be about six times larger in horn-on running mode, compared to horn-off running mode. Therefore, it is necessary to accurately simulate the motion of charged particles in the field, in order to obtain reliable flux predictions.

The transportation algorithms through a non-uniform magnetic field region used by the beam Monte Carlo simulation have been validated via an independent tracking algorithm. The simple test case considered here is that of a magnetic field region that is similar to the MiniBooNE horn one, with an azimuthal fielld of magnitude $B = \mu_0 I/(2\pi r)$, where $\mu_0 = 4\pi \cdot 10^{-7}$ is the permittivity of free space, $I =$170 kA and $r = \sqrt{x^2 + y^2}$, in the region 2.2 cm $< r <$ 30 cm, $0 < z <$ 180 cm, and zero magnetic field otherwise. Positive pions of various momenta, produced at $(x = 0, y = 0, z = 30$ cm$)$ and with an initial momentum direction of $p_x/p_z = 1/8$, $p_y = 0$, are tracked through this simple geometry. The particle trajectories are described by the
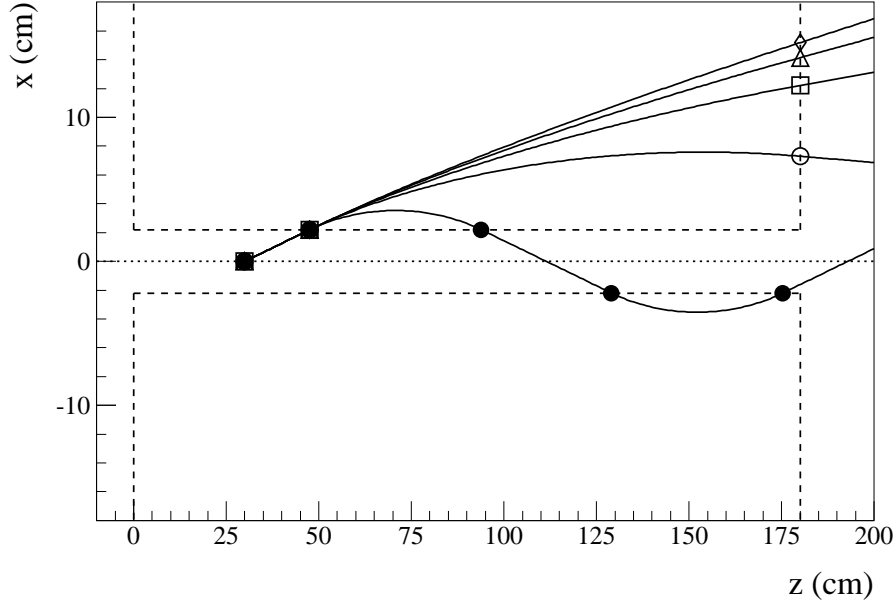
Figure 4.7: *Trajectories in the horn magnetic field for 0.5, 1.5, 2.5, 3.5, and 4.5 GeV kinetic energy π^+'s, with initial conditions: ($x_0 = 0$, $z_0 = 30$ cm, $p_{x,0}/p_{z,0} = 1/8$). The points are from a beam Monte Carlo simulation, the dashed curves from the solution of Eq. 4.3 discussed in the text.*

following system of two coupled, second-order differential equations:

$$
\begin{cases}
\ddot{x}(t) = \dfrac{c_B}{x(t)}\dot{z}(t), & \dot{x}(0) = v_0 \sin\theta, \quad x(0) = x_0 \\[2ex]
\ddot{z}(t) = -\dfrac{c_B}{x(t)}\dot{x}(t), & \dot{z}(0) = v_0 \cos\theta, \quad z(0) = z_0
\end{cases}
\tag{4.3}
$$

where, in SI units:

$$
c_B = \frac{\mu_0 I}{2\pi} \cdot \frac{q}{m_\pi \gamma}
\tag{4.4}
$$

where μ_0 and I are defined above, q is the (positive) electron charge, m_π the π^+ mass, γ is the relativistic γ factor for the pion, $v_0 = c\sqrt{\gamma^2 - 1}/\gamma$, $\theta = \arctan(1/8)$ in this case.

The particle trajectories as calculated by the beam Monte Carlo simulation, and by an independent tracking algorithm based on a Runge-Kutta-Nystrom numerical integration [16] of Eq. 4.3, are shown to be consistent with each other in Fig.4.7, for pions of various momenta.
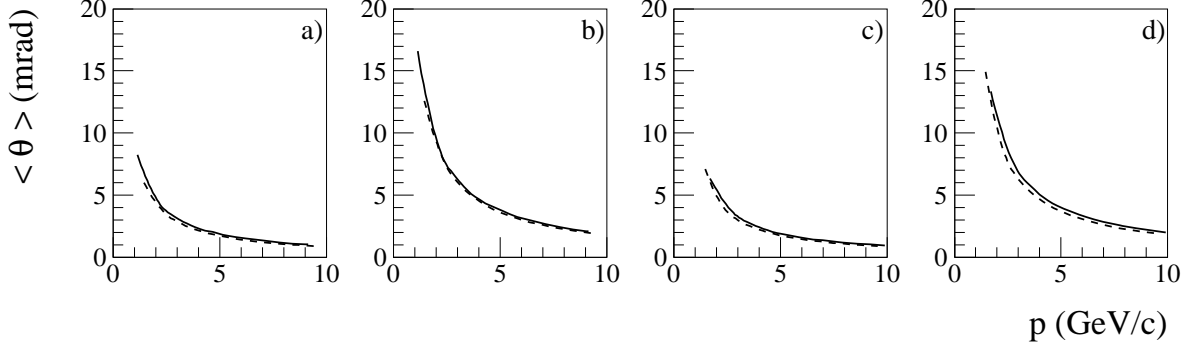
Figure 4.8: *Multiple Coulomb scattering results obtained from a simulation of 10 cm of material, as a function of projectile momentum p. From left to right: multiple Coulomb scattering of π^+ in Be, π^+ in Al, p in Be, p in Al. The average projectile deflection angle, $\langle\theta\rangle$, is shown. The dashed curves, almost indistinguishable from the beam Monte Carlo solid curves, show the predictions from Eqs. 4.5 and 4.6 in the text.*

4.5.2   Multiple Coulomb scattering

Any charged particle traversing a material undergoes many small electromagnetic scatters that can be described cumulatively, at a macroscopic level. The beam Monte Carlo simulation uses the Lewis formalism to simulate multiple Coulomb scattering. The multiple Coulomb scattering angle distributions for pions and protons, simulated by the beam Monte Carlo program through 10 cm of Beryllium and Aluminum materials, are shown in Fig.4.8 as a function of projectile momenta. This material thickness is chosen in this example because it is comparable to the materials traversed by protons and pions yielding muon neutrinos at MiniBooNE (see Tab. 4.4).

Multiple Coulomb scattering is more important for low-momentum than for high-momentum projectiles, for Aluminum than Beryllium, and for protons than for pions. Typical scattering angles over 10 cm of material traversed are between 1 and 20 mrad.

The beam Monte Carlo results can be confronted with the Highland formula from

Ref. [1], describing the average multiple Coulomb scattering angle $\langle\theta\rangle$:

$$\langle\theta\rangle_H = \sqrt{\frac{\pi}{2}}\sigma_\theta \tag{4.5}$$

where:

$$\sigma_\theta = \frac{13.6 \text{ MeV}}{\beta c p}\sqrt{z/X_0}[1 + 0.038\ln(z/X_0)] \tag{4.6}$$

In Eq.4.6, βc is the projectile velocity, p its momentum, $z \simeq 10$ cm is the material traversed, X_0 is the material radiation length, equal to 35.28 cm for Beryllium and 8.90 cm for Aluminum [1]. The dashed curves in Fig. 4.8 show the average deflection angle due to multiple Coulomb scattering as predicted by the Highland formula of Eqs. 4.5 and 4.6, and good agreement with the beam Monte Carlo simulations is obtained.

4.5.3 Ionisation by charged hadrons

The last electromagnetic process discussed here is energy loss by charged hadrons. In the beam Monte Carlo simulation, this process simulates both the continuous energy loss due to ionisation and atomic excitation via the Bethe-Bloch formula, as well as the "discrete" part of the ionisation via δ-ray emission. As for multiple Coulomb sacattering processes, the macroscopic effects due to energy loss are quantified for particle crossing $z = 10$ cm of Beryllium and Aluminum materials, and the results from beam Monte Carlo simulations are shown in Fig. 4.9. In Figure 4.9, we define Δ as the projectile energy loss across the material thickness:

$$\Delta \equiv -\int_0^{10 \text{ cm}} \frac{dE}{dz}dz \tag{4.7}$$

The energy loss results in Fig. 4.9 can be compared with the Bethe-Bloch formula given in [1], for π^+ or p projectiles in Beryllium (Aluminum):

$$-\frac{dE}{dx} = \rho K z^2 \frac{Z}{A}\frac{1}{\beta^2}[\frac{1}{2}\ln\frac{2m_e c^2 \beta^2 \gamma^2 T_{max}}{I^2} - \beta^2 - \frac{\delta}{2}] \tag{4.8}$$
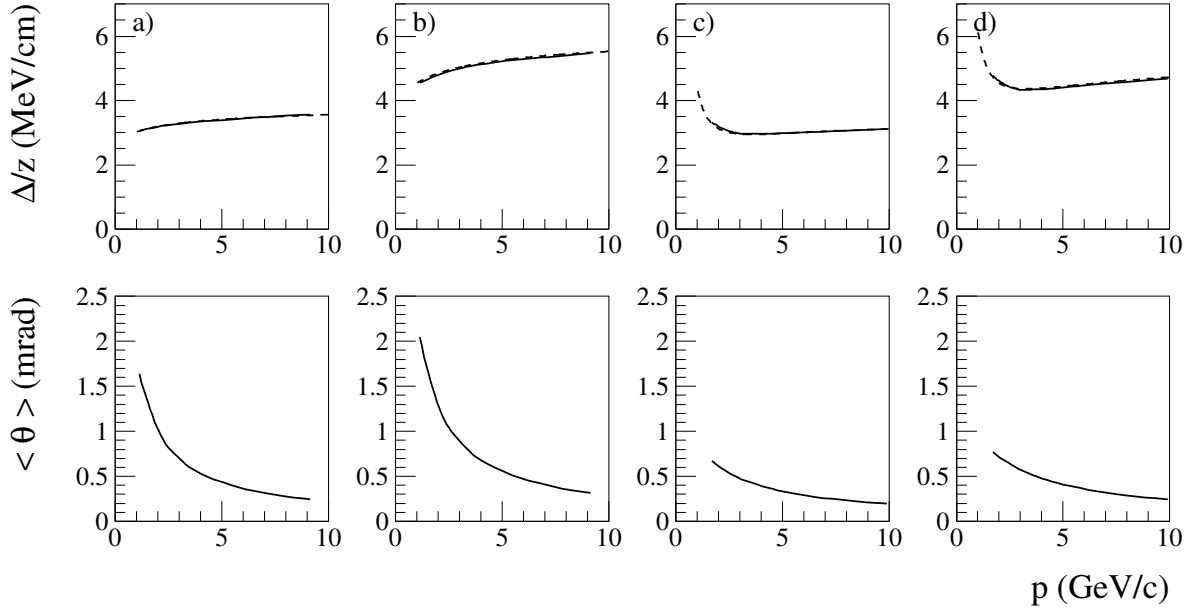
Figure 4.9: *Energy loss results obtained from a simulation of 10 cm of material, as a function of projectile momentum p. From left to right: energy loss of π^+ in Be, π^+ in Al, p in Be, p in Al. From top to bottom: average energy loss per unit material traversed, Δ/z; average projectile deflection angle, $\langle\theta\rangle$. The dashed curves, almost indistinguishable from the beam Monte Carlo solid curves, show the predictions from Eqs. 4.8 and 4.9 in the text.*

where $K = 0.307075 \ MeV \ g^{-1} \ mol^{-1}$, $z = 1$ is the projectile electric charge in units of e, $Z = 4$ (13) is the target electric charge in units of e, $A = 9.01$ (26.98) is the target atomic weight in units of g/mol, β is the projectile's velocity in units of c, $m_e c^2 = 0.511$ MeV is the electron mass, $\gamma = (1 - \beta^2)^{-1/2}$, $T_{max} = 2m_e c^2 \beta^2 \gamma^2/(1 + 2\gamma m_e/M + (m_e/M)^2)$ is the maximum kinetic energy which can be imparted to a free electron in a single collision, $M = 139.57$ or $938.27 \ MeV/c^2$ is the projectile's mass, $I = 63.7$ (166.0) eV is the mean excitation energy, and δ is the density effect correction to ionization energy loss, given by:

$$\delta = \begin{cases} 2(\ln 10)x - \bar{C} & \text{,if } x \geq x_1; \\ 2(\ln 10)x - \bar{C} + a(x_1 - x)^k & \text{,if } x_0 \leq x < x_1; \\ \delta_0 10^{2(x-x_0)} & \text{,if } x < x_0 \end{cases} \tag{4.9}$$

where $x = \log_{10}(p/Mc)$, x_0 =0.0592 (0.1708), x_1 =1.6922 (3.0127), $\bar{C}$ =2.7847 (4.2395), a =0.80392 (0.08024), k =2.4339 (3.6345), δ_0=0.14 (0.12) [1]. The expected energy loss given by Eqs. 4.8 and 4.9 is consistent with the beam Monte Carlo assumptions.

Figure 4.9 also shows the mean projectile deflection angles after traversing z =10 cm of material. These angles are very small, of the order of 1 mrad, and negligible with respect to the deflection angles due to nuclear elastic scattering or multiple Coulomb scattering.

4.6 Neutrinos from meson and muon decays

Neutrinos reaching the MiniBooNE detector are produced via the decays of charged pions, kaons, and muons. Particle lifetimes, decay branching ratios, Lorentz boosts, and center-of-mass kinematics of the neutrinos produced in the decays affect the neutrino flux predictions, and are discussed here.

The neutrino parent lifetimes and branching ratios used in the simulation are given in Tab. 4.9, for π^+, K^+, K_L^0, and μ^+ neutrino parents, and the corresponding decays of negatively-charged particles are also simulated. Given the relevance of decays yielding electron neutrinos for the MiniBooNE $\nu_\mu \to \nu_e$ search, the GEANT4 built-in decay channels and branching ratios have been updated to yield more accurate electron neutrino predictions.

The effect of Lorentz boosts is shown in Fig. 4.10. Figure 4.10a) shows the decay length λ_{decay} as a function of neutrino parent momentum p. The data points from beam Monte Carlo simulations match well the $\gamma\beta c\tau$ expectations, where the lifetime τ for a neutrino parent type is the one given in Tab. 4.9, and $\gamma\beta = p/m$, where m is the neutrino parent mass. Also, Lorentz boosts are applied in the simulation to determine the neutrino kinematics in the laboratory frame, once the neutrino kinematics is generated in the parent rest frame. In Figure 4.10b), we show the

Particle	Lifetime (ns)	Decay mode	Branching ratio (%)
π^+	26.03	$\mu^+\nu_\mu$	99.9877
		$e^+\nu_e$	0.0123
K^+	12.37	$\mu^+\nu_\mu$	63.17
		$\pi^+\pi^0$	21.2
		$\pi^+\pi^+\pi^-$	5.6
		$\pi^0 e^+\nu_e$	5.13
		$\pi^0\mu^+\nu_\mu$	3.2
		$\pi^+\pi^0\pi^0$	1.7
K_L^0	51.70	$\pi^0\pi^0\pi^0$	19.45
		$\pi^- e^+\nu_e$	20.4
		$\pi^+ e^-\bar{\nu}_e$	20.27
		$\pi^-\mu^+\nu_\mu$	13.55
		$\pi^+\mu^-\bar{\nu}_\mu$	13.46
		$\pi^0\pi^+\pi^-$	12.87
μ^+	2197.03	$e^+\nu_e\bar{\nu}_\mu$	100.0

Table 4.9: *Particle lifetimes, and* `BooNEG4Beam` *decay modes and branching ratios.*

neutrino energy as a function of the parent neutrino momentum p in the laboratory frame, for $\pi^+ \to \mu^+ \to \nu_\mu$ decays and for neutrinos crossing a disk of radius R_{det} =6.1 m and located L =541 m from the pion production location, that is for the neutrino phase space of relevance to MiniBooNE. The dashed curves in Fig. 4.10b) correspond to the maximum and minimum neutrino energies, given by:

$$\begin{cases} E_{\nu,max} = \gamma E_\nu^{CM}(1+\beta) \\ E_{\nu,min} = \gamma E_\nu^{CM}(1+\beta\cos\theta_{max}^{CM}) \end{cases} \tag{4.10}$$

where: $E_\nu^{CM} = (m_\pi^2 - m_\mu^2)/(2m_\pi)$ is the neutrino energy in the pion rest frame, $\gamma = \sqrt{1 + (p/m_\pi)^2}$, $\beta = \sqrt{\gamma^2 - 1}/\gamma$, $\theta_{max}^{CM} = 2\arctan(\gamma\tan\theta_{max})$ and $\theta_{max} = \arctan(R_{det}/L)$
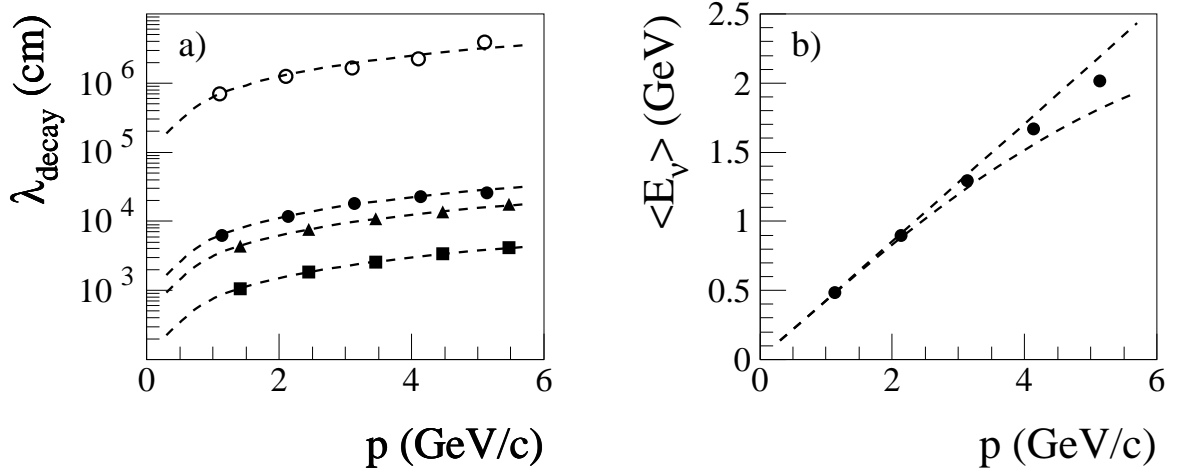
Figure 4.10: *Validation of decay routines in the beam Monte Carlo simulation. Fig. 4.10a) shows the decay length λ_{decay} as a function of the parent momentum p, for (from bottom to top) K^+, π^+, K^0_L, μ^+ parents. Fig. 4.10b) shows the average neutrino energy in $\pi^+ \to \nu_\mu \to \mu^+$ decays as a function of pion momentum p, for neutrinos crossing the MiniBooNE detector. The points are the results from beam Monte Carlo simulations, the dashed curves are the minimum and maximum neutrino energies discussed in the text.*

are the angles between the pion direction and the neutrino directions in the pion rest frame and in the laboratory frame, respectively. From Fig. 4.10b), one finds that the average neutrino energy predicted by the beam Monte Carlo simulation lies approximately in between the minimum and maximum energies from Eq. 4.10. This is the expected result, given the isotropic neutrino angular distribution in the pion rest frame: in this case, $dN/d\cos\theta^{CM} = const$ in the pion rest frame implies $dN/dE_\nu = const$ in the laboratory frame, for fixed pion momenta.

Finally, we discuss the kinematics of neutrino decays in the rest frame of the neutrino parents, for the most relevant decays yielding muon and electron neutrinos, separately.
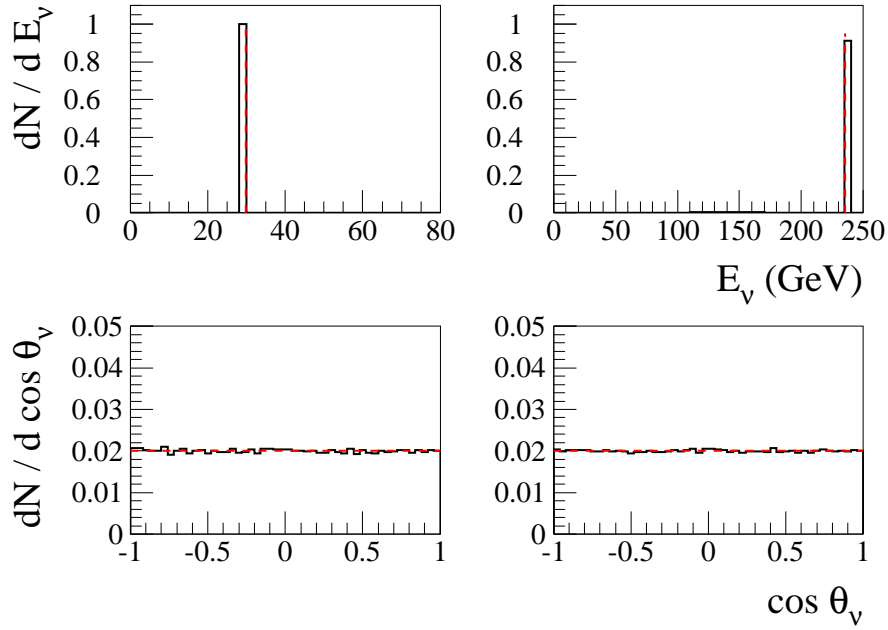
Figure 4.11: *Muon neutrino kinematic distributions in the neutrino parent rest frame. The top row shows the neutrino energy distribution, the bottom row shows the neutrino angular distribution with respect to the z-direction in the laboratory frame. The left column refers to π^+ decays, the right column to K^+ decays. The histograms are the results of beam Monte Carlo simulations, the dashed curves are the expectations discussed in the text.*

4.6.1 Decays into muon neutrinos

Muon neutrinos reaching MiniBooNE are mostly produced by π^+ decays, with a non-negligible contribution from K^+ decays (see Tab. 4.3). The histograms in Fig. 4.11 show the muon neutrino energy and angular distributions in π^+ and K^+ decays at rest. The angular distributions are flat, while the neutrino energy from the $\pi^+/K^+ \to \mu^+\nu_\mu$ two-body decays is $(m_{\pi/K} - m_\mu)/(2m_{\pi/K})$. For Kaon decays, a small fraction ($\simeq 5\%$) of muon neutrinos is simulated with a continuous energy distribution from $K^+ \to \pi^0\mu^+\nu_\mu$ three-body decays (see Tab. 4.9).
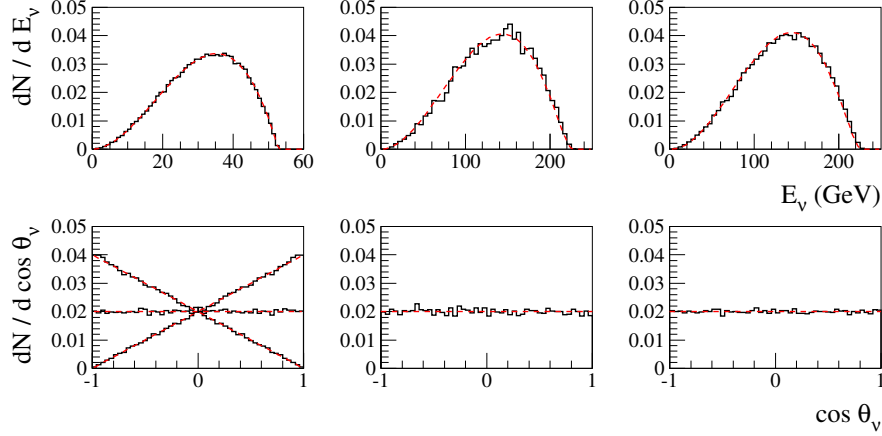
Figure 4.12: *Electron neutrino kinematic distributions in the neutrino parent rest frame. The left column refers to μ^+ decays, the middle column to K^+ decays, and the right column to K_L^0 decays. The top row shows the neutrino energy distribution, the bottom row shows the neutrino angular distribution with respect to the z-direction in the lab frame, defined as the beam direction. The three curves for muons correspond to the cases: $P_z = -1, 0, +1$, where P_z is the projection along z of the muon polarization vector in the muon rest frame. The histograms are the results of beam Monte Carlo simulations, the dashed curves are the expectations discussed in the text.*

4.6.2 Decays into electron neutrinos

Muon decays and leptonic decays of Kaons (both charged and neutral) are predicted to yield almost the entire electron neutrino flux at MiniBooNE (see Tab. 4.3). The neutrino energy and angular distribution from μ^+ decays is, neglecting terms proportional to the electron mass [17]:

$$\frac{dN}{dx\, d\cos\theta_\nu} \propto \frac{12x^2}{4\pi}(1-x)(1 \mp P_z \cos\theta) \tag{4.11}$$

where $\cos\theta_\nu$ is the neutrino emission angle with respect to the beam direction z, P_z is the projection along z of the muon polarization vector in the muon rest frame, and $x = 2E_\nu/m_\mu$, with $0 < x < 1$. In $\pi^+ \to \mu^+ \to \nu_e$ decays, the muon polarization in the muon rest frame is calculated from the known muon polarization in the pion rest frame, and boosting the polarizaton vector into the muon rest frame.

For the Kaon three-body decays yielding electron neutrinos (that is, $K \to \pi e \nu_e$, or K_{e3} decays), the neutrino angular distribution, in the Kaon rest frame and with respect to the beam direction, are flat. Assuming that only the vector current contributes to the Kaon semileptonic decay matrix element, and neglecting electron mass terms, the neutrino energy distribution in the Kaon rest frame is [18]:

$$\frac{dN}{dE_\nu} \propto \int_{E_{e,-}}^{E_{e,+}} dE_e (2E_e E_\nu - m_k E'_\pi) |f_+(t)|^2 \tag{4.12}$$

where all quantities refer to the Kaon rest frame, E_e is the electron energy, $E'_\pi \equiv E_\pi^{max} - E_\pi$, $E_\pi^{max} = (m_K^2 + m_\pi^2)/(2m_K)$ is the maximum energy that can be transferred to the pion, E_π is the pion energy, f_+ is a form factor depending only on the square of the four-momentum transfer to the leptons, $t = (p_k - p_\pi)^2 = m_k^2 + m_\pi^2 - 2m_k E_\pi$, and $E_{e,\pm}$ are integration limits on the electron energy:

$$\begin{cases} E_{e,-} = \frac{m_K^2 - m_\pi^2}{2m_k} - E_\nu \\ E_{e,+} = \frac{1}{2}(m_k - \frac{m_\pi^2}{m_k - 2E_\nu}) \end{cases} \tag{4.13}$$

The beam Monte Carlo simulation also assumes, as customarily done, a linear dependence of the form factor f_+ on t:

$$f_+(t) \propto (1 + \lambda_+ t/m_\pi^2) \tag{4.14}$$

For K_{e3}^+ (K_{e3}^0) decays, the coefficient λ_+ for the linear expansion of the form factor is 0.0277 (0.0291) [1].

The expected kinematics for electron neutrinos in muon decays and semileptonic Kaon decays described above are shown with dashed lines in Fig. 4.12, and agree well with the beam Monte Carlo results.

4.7 Neutrino flux predictions at the MiniBooNE detector

In this Section we present the results of the beam Monte Carlo simulations, that is the neutrino flux predictions at the MiniBooNE detector location, as a function of

neutrino energy and for all relevant neutrino flavors.

Table 4.10 shows a summary on neutrino flux predictions, given in terms of

Neutrino Flavor	Neutrino Parent	$\phi \ (cm^{-2}pot^{-1})$	$\langle E_\nu \rangle$
all	all	$5.22 \cdot 10^{-10}$	0.760
ν_μ	all	$4.84 \cdot 10^{-10}$	0.778
ν_μ	π^+	$4.69 \cdot 10^{-10}$	0.734
ν_μ	K^+	$1.42 \cdot 10^{-11}$	2.250
$\bar{\nu}_\mu$	all	$3.47 \cdot 10^{-11}$	0.488
$\bar{\nu}_\mu$	π^-	$3.24 \cdot 10^{-11}$	0.470
ν_e	all	$3.07 \cdot 10^{-12}$	0.939
ν_e	μ^+	$1.70 \cdot 10^{-12}$	0.665
ν_e	μ^+	$1.07 \cdot 10^{-12}$	1.321
$\bar{\nu}_e$	all	$3.44 \cdot 10^{-13}$	0.888
$\bar{\nu}_e$	K^0_L	$2.55 \cdot 10^{-13}$	1.032

Table 4.10: *Summary of neutrino flux predictions at MiniBooNE, for neutrino running mode. The fluxes ϕ, as well as the neutrino energy $\langle E_\nu \rangle$ averaged over the flux distribution, are given. The most important contributions from the various neutrino flavors and neutrino parent types are shown.*

total flux and mean neutrino energy averaged over the flux distributions, for the various neutrino flavors and for the most important neutrino parent types. The overall neutrino flux prediction is $5.22 \cdot 10^{-10} \ cm^{-2}pot^{-1}$, with a mean neutrino energy of 0.76 GeV. The flux prediction is $4.84 \cdot 10^{-10} \ cm^{-2}pot^{-1}$ for muon neutrinos, $3.47 \cdot 10^{-11} \ cm^{-2}pot^{-1}$ for muon antineutrinos, $3.07 \cdot 10^{-12} \ cm^{-2}pot^{-1}$ for electron neutrinos, $3.44 \cdot 10^{-13} \ cm^{-2}pot^{-1}$ for electron antineutrinos, yielding a 0.6% ν_e/ν_μ flux ratio, and a 0.7% $(\nu_e + \bar{\nu}_e)/(\nu_\mu + \bar{\nu}_\mu)$ flux ratio.

Figure 4.13 shows the neutrino energy distributions for muon neutrinos, muon antineutrinos, and electron neutrinos. Figure 4.14 shows the muon neutrino energy
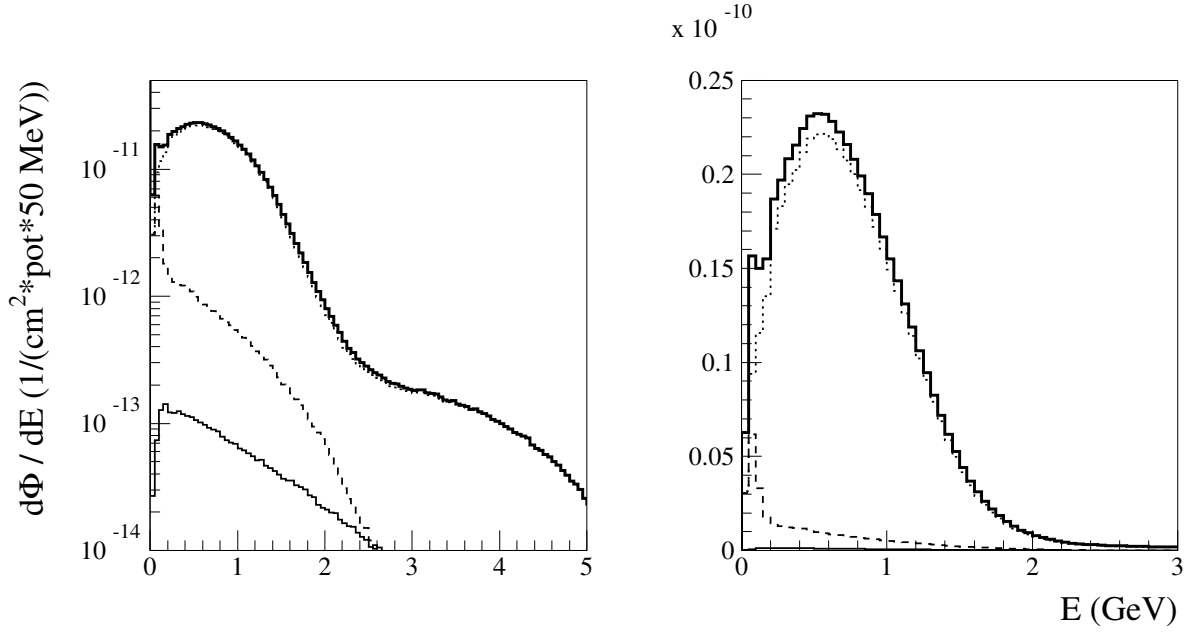
Figure 4.13: *Predicted neutrino flux as a function of neutrino energy, for all neutrinos reaching MiniBooNE, in neutrino running mode. The thick solid histogram is for all neutrinos, the thin solid histogram for ν_e, the dashed histogram for $\bar{\nu}_\mu$, the dotted histogram for ν_μ. The fluxes are shown on a logarithmic scale on the left, and on a linear scale on the right.*

distribution, together with the partial contributions from π^+ and K^+ decays. Figure 4.15 shows the electron neutrino energy distribution, together with the partial contributions from μ^+, K^+, and K^0_L decays.
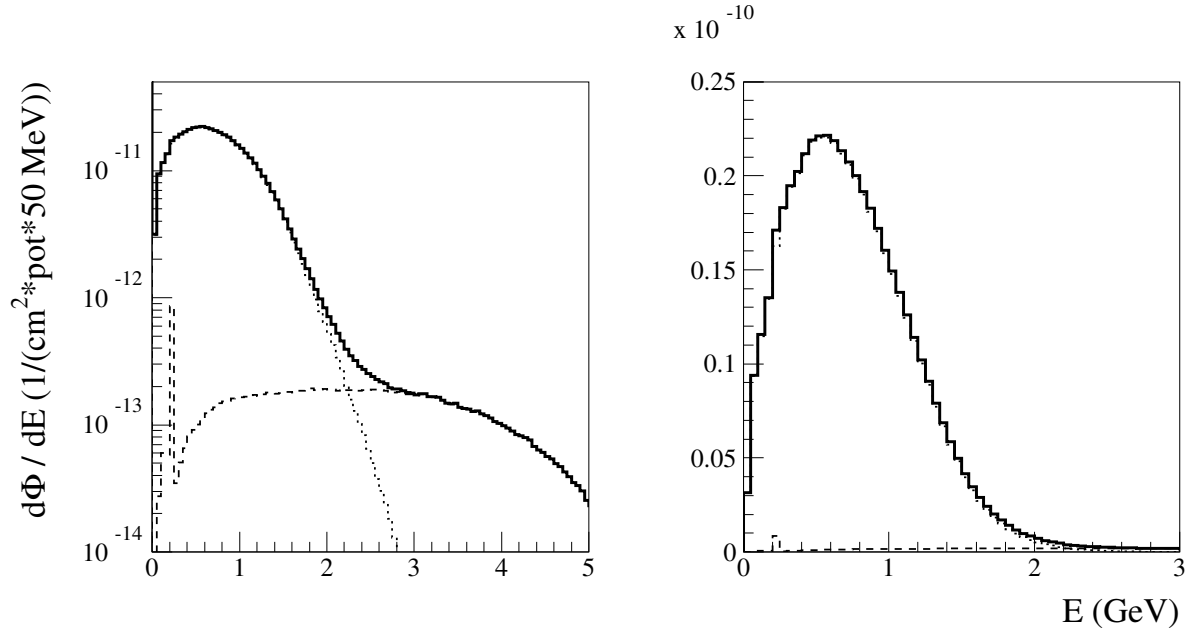
Figure 4.14: *Predicted muon neutrino flux as a function of neutrino energy, for all muon neutrinos reaching MiniBooNE, in neutrino running mode. The solid histogram is for all muon neutrinos, the dashed histogram for muon neutrinos from K^+ decay, the dotted histogram for muon neutrinos from π^+ decay. The fluxes are shown on a logarithmic scale on the left, and on a linear scale on the right.*
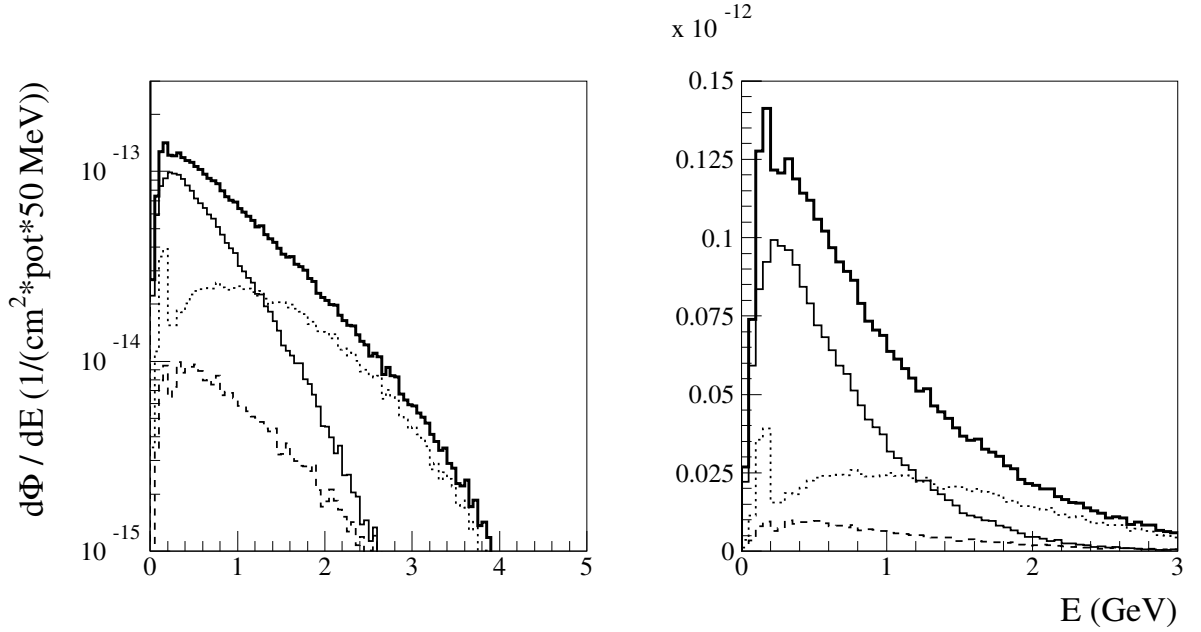
Figure 4.15: *Predicted electron neutrino flux as a function of neutrino energy, for all electron neutrinos reaching MiniBooNE, in neutrino running mode. The thick solid histogram is for all electron neutrinos, the thin solid histogram for electron neutrinos from μ^+ decay, the dashed histogram for electron neutrinos from K^+ decay, the dotted histogram for electron neutrinos from K_L^0 decay. The fluxes are shown on a logarithmic scale on the left, and on a linear scale on the right.*

Bibliography

[1] S. Eidelman *et al.* [Particle Data Group Collaboration], Phys. Lett. B **592**, 1 (2004).

[2] S. Agostinelli *et al.* [GEANT4 Collaboration], Nucl. Instrum. Meth. A **506**, 250 (2003).

[3] `http://wwwasd.web.cern.ch/wwwasd/geant4/G4UsersDocuments/Overview/html/`

[4] J. Link and J. Monroe, private communication. Publication in preparation.

[5] N. V. Mokhov, FERMILAB-FN-0628 (1995).

[6] N. V. Mokhov, K. K. Gudima, C. C. James *et al.*, FERMILAB-Conf-04/053 (2004).

[7] Y. Cho *et al.*, Phys. Rev. D **4**, 1967 (1971).

[8] I. A. Vorontsov, V. A. Ergakov, G. A. Safronov, A. A. Sibirtsev, G. N. Smirnov, N. V. Stepanov and Y. V. Trebukhovsky, "Measurement Of Inclusive Cross-Sections Pi-, Pi+, P, H-2, H-3, He-3 At Angle ITEP-85-1983

[9] J. V. Allaby *et al.*, Phys. Lett. B **30**, 549 (1969).

[10] G. J. Marmer and D. E. Lundquist, Phys. Rev. D **3**, 1089 (1971).

[11] Y. D. Aleshin, I. A. Drabkin and V. V. Kolesnikov, ITEP-80-1977

[12] HARP Collaboration, CERN-SPSC-2004-018

[13] V. V. Gachurin *et al.*, ITEP-59-1985

[14] Lykhachev, **Zh. Eksp. Teor. Fiz. 41** (1981) 39;

[15] Afonasiev, **Yad. Fiz. 47** (1988) 1656.

[16] `http://cernlib.web.cern.ch/cernlib/overview.html`

[17] S. Geer, Phys. Rev. D **57**, 6989 (1998) [Erratum-ibid. D **59**, 039903 (1999)] [arXiv:hep-ph/9712290].

[18] L. M. Chounet, J. M. Gaillard and M. K. Gillard, Phys. Rept. **4**, 199 (1972).